RSC Advances

PAPER

View Article Online
View Journal | View Issue

Cite this: *RSC Adv.*, 2018, **8**, 30191

Novel $SrMg_2La_2W_2O_{12}:Mn^{4+}$ far-red phosphors with high quantum efficiency and thermal stability towards applications in indoor plant cultivation LEDs

Shaoying Wang, Qi Sun, Balaji Devakumar, Liangling Sun, Jia Liang and Xiaoyong Huang *

Received 19th July 2018
Accepted 21st August 2018

DOI: 10.1039/c8ra06134c

rsc.li/rsc-advances

Novel Mn^{4+}-activated far-red emitting $SrMg_2La_2W_2O_{12}$ (SMLW) phosphors were prepared by a conventional high-temperature solid-state reaction method. The SMLW:Mn^{4+} phosphors showed a broad excitation band peaking at around 344 nm and 469 nm in the range of 300–550 nm. Under 344 nm near-ultraviolet light or 469 nm blue light, the phosphors exhibited a far-red emission band in the 650–780 nm range centered at about 708 nm. The optimal Mn^{4+} doping concentration in the SMLW host was 0.2 mol% and the CIE chromaticity coordinates of SMLW:0.2% Mn^{4+} phosphors were calculated to be (0.7322, 0.2678). In addition, the influences of crystal field strength and nephelauxetic effect on the emission energy of Mn^{4+} ions were also investigated. Moreover, the internal quantum efficiency of SMLW:0.2% Mn^{4+} phosphors reached as high as 88% and they also possessed good thermal stability. Specifically, the emission intensity at 423 K still maintained about 57.5% of the initial value at 303 K. Finally, a far-red light-emitting diode (LED) lamp was fabricated by using a 365 nm near-ultraviolet emitting LED chip combined with the as-obtained SMLW:0.2% Mn^{4+} far-red phosphors.

1. Introduction

Nowadays, indoor plant cultivation has gained much attention and it is becoming a powerful solution to the global food problem for the reason that a controlled environment (*e.g.*, filtered air, steady temperature, and special growth media) can allow plants to grow steadily without being affected by terrible weather such as drought, storms, hail, torrential rain, fog, and haze.[1–5] An artificial light source for indoor plant cultivation has become an important condition for efficient production, because cultivating plants in an artificial lighting environment can make up for the deficiency of bad climate, regulate the growth cycle on demand, and improve the yield and quality of crops.[6,7]

Solid-state phosphor-converted light-emitting diodes (LEDs) have been considered as a good kind of artificial light source for indoor plant cultivation owing to their outstanding advantages including small size, long working time, good stability, high photoelectric conversion efficiency, and environmental friendliness compared with traditional incandescent and fluorescent lamps.[8–22] Besides, the light quality of the artificial light source is one of the essential factors affecting the development of plants. The absorption of light by plants is not full-wavelength but selective. Blue light around 450 nm (440–480 nm) is beneficial to the growth of stem and the morphogenesis of leaf; red light around 660 nm (620–690 nm) promotes the synthesis of plant carbohydrates, blossoming, and yielding fruits; while far-red light around 730 nm (700–740 nm) contributes to the photosynthesis.[23–25] In addition, in the light reaction of plants, the primary light receptor is phytochrome, which is extremely sensitive to red light and far-red light, thus including P_R and P_{FR}, respectively.[26] The effects of phytochrome on plant morphology include seed germination, de-etiolation, stem elongation, leaf expansion, and flowering induction. Therefore, it plays an important role in the whole process of plant growth and development from germination to maturity.[27] Consequently, it is very urgent to develop far-red emitting phosphors that can be used in solid-state phosphor-converted LEDs as artificial light source for indoor plant cultivation.

Mn^{4+} ions doped red phosphors have some advantages such as suitable spectra, simple synthesis procedure, as well as the cheap and readily available raw materials compared with the traditional rare-earth ions (such as Eu^{3+}/Eu^{2+}) doped red phosphors.[28] In detail, Mn^{4+} ions with a $3d^3$ electronic configuration belong to transition mental ions, while the phosphors doped with Mn^{4+} ions can be excited by near-ultraviolet (near-UV) and blue light, and show far-red emission ranging from 620 to 750 nm centered at about 660 nm owing to the $^2E_g \rightarrow {}^4A_{2g}$

Key Lab of Advanced Transducers and Intelligent Control System, Ministry of Education and Shanxi Province, College of Physics and Optoelectronics, Taiyuan University of Technology, Taiyuan 030024, P. R. China. E-mail: huangxy04@126.com

transition of Mn^{4+} ions.[2,12,29–33] Besides, the crystal field environment is greatly important to the optical properties of Mn^{4+} ions and Mn^{4+} ions can occupy the cation sites of octahedrons in the host.[34] So, finding a novel host material, which can provide octahedral sites for Mn^{4+} ions, is also very significant. Tungstates are good host materials used in phosphors because they have many merits including low price, good chemical stability, and outstanding optical properties.[35,36] Recently, Mn^{4+} ions activated tungstates far-red emitting phosphors have been reported such as $Ca_3La_2W_2O_{12}$:Mn^{4+},[3] Sr_2ZnWO_6:Mn^{4+},[37] and $NaLaMgWO_6$:Mn^{4+}.[38] In addition, some phosphors based on tungstate $SrMg_2La_2W_2O_{12}$ (SMLW) have been investigated previously, such as SMLW:Tb^{3+},Eu^{3+},[39] SMLW:Dy^{3+},Tm^{3+},[40] and SMLW:Tb^{3+},Sm^{3+},Tm^{3+},[41] and SMLW including [WO_6] and [MgO_6] octahedrons can provide octahedral sites, which indicates that SMLW is a suitable host material for Mn^{4+} ions doped phosphors.

In this work, a series of novel Mn^{4+}-activated SMLW phosphors were prepared by a conventional high-temperature solid-state reaction method. It was discovered that SMLW:Mn^{4+} phosphors can be excited at 344 nm or 469 nm and exhibited a far-red emission band in the 650–780 nm range centered at about 708 nm, which matched well with the absorption band of phytochrome P_{FR}. The optimal Mn^{4+} doping concentration in the SMLW host was 0.2%. And the full width at half maximum (FWHM) of the far-red emission band was determined to be about 37 nm. Moreover, the IQE of SMLW:0.2% Mn^{4+} phosphors reached as high as 88% and they also possessed good thermal stability. Finally, a far-red LED device was fabricated by coating as-prepared SMLW:0.2% Mn^{4+} far-red phosphors on a 365 nm near-UV emitting LED chip. The results suggested that the far-red emitting SMLW:Mn^{4+} phosphors were potential luminescent materials that can be applied for indoor plant cultivation LEDs.

2. Experimental

A series of $SrMg_2La_2W_{2(1-x)}O_{12}$:$xMn^{4+}$ (SMLW:xMn^{4+}; $x = 0.1\%$, 0.2%, 0.4%, 0.6%, 0.8%, and 1.0%) phosphors were successfully prepared by a conventional high-temperature solid-state reaction method. $SrCO_3$ (analytical reagent, AR), MgO (AR), La_2O_3 (99.99%), $(NH_4)_6H_2W_{12}O_{40}$ (AR), $MnCO_3$ (AR) were used as raw materials. They were weighed on the basis of stoichiometric ratio and ground in an agate mortar to make them uniform. Then, these mixtures were put into the alumina crucibles and pre-fired at 600 °C for 4 h in the air, after that they were ground again and then sintered at 1200 °C for 6 h in the air. When the samples were cooled down to room temperature, they were ground again and gathered for further characterization.

The phase purity of the phosphors was tested by X-ray diffraction (XRD) patterns recorded on a Bruker D8 Focus diffractometer with Cu Kα radiation. The morphology properties of the samples were obtained by using a field-emission scanning electron microscope (FE-SEM; TESCAN MAIA3). The room-temperature photoluminescence (PL) and photoluminescence excitation (PLE) spectra were measured by Edinburgh FS5 spectrometer equipped with a 150 W continued-wavelength xenon lamp. The decay times of phosphors were recorded on an Edinburgh FS5 spectrometer with a pulsed xenon lamp. Temperature-dependent PL spectra were also measured by using the Edinburgh FS5 spectrometer equipped with a temperature controller. The IQE was tested on an Edinburgh FS5 spectrometer equipped with an integrating sphere coated with $BaSO_4$.

3. Results and discussion

The Rietveld refinement for the XRD patterns of SMLW:0.2% Mn^{4+} was analyzed to study its crystal structure and the site occupancy, as shown in Fig. 1(a). According to the refinement results, we can find that the crystal structure of SMLW:0.2% Mn^{4+} belongs to orthorhombic crystal system with the $P222$ space group, and the cell parameters were calculated to be $a = 7.8465$ Å, $b = 7.8627$ Å, $c = 7.9014$ Å, $\alpha = 90°$, $\beta = 90°$, $\gamma = 90°$, and $V = 487.47$ Å^3. The crystal structure of SMLW:0.2% Mn^{4+} included [MgO_6] and [WO_6] octahedrons formed by Mg and W atoms coordinated with six oxygen atoms around respectively, as can be seen in Fig. 1(b). As well-known, Mn^{4+} ions can occupy the cation sites of octahedrons.[42] In this work, Mn^{4+} ions were more likely to occupy the site of W^{6+} because the radius of Mn^{4+} ion (0.53 Å) is much closer to that of W^{6+} ion (0.62 Å) than Mg^{2+} ion (0.72 Å).[12,37]

In order to study the possibility that Mn^{4+} ions can substitute W^{6+} ions in the host, we can calculate the radius percentage difference between the doped ions Mn^{4+} and the substituted ions W^{6+} in SMLW host by using the following formula:[43]

$$D_r = \frac{R_s - R_d}{R_s} \times 100\% \quad (1)$$

where D_r refers to the radius percentage difference; R_s and R_d represent the radius of the substituted ions in the host and the doped ions, respectively. Therefore, according to the ionic radii mentioned above, the value of D_r was calculated to be 15%, and it is much smaller than 30%, which indicated that the doped Mn^{4+} ions could legitimately replace the sites of W^{6+} ions.

Fig. 2(a) shows the XRD patterns of the as-prepared SMLW:xMn^{4+} ($x = 0.1\%$, 0.2%, 0.4%, 0.6%, 0.8%, and 1.0%) and the standard PDF card of SMLW (JCPDS # 35-0259). The XRD patterns of the samples matched well with the standard data of SMLW (JCPDS # 35-0259) except that there were two weak impurity peaks due to the $SrWO_4$ (JCPDS # 08-0490). This result indicated that doping Mn^{4+} into SMLW did not make significant changes to the host crystal structure. According to the local XRD patterns in the 2θ range of 30.5–34.5 degree shown in Fig. 2(b), we can find that the XRD diffraction peaks slightly shifted to the larger angle in comparison with the standard data when the Mn^{4+} doping concentration was increased for the reason that the smaller ions Mn^{4+} ($r = 0.53$ Å) substituted larger ions W^{6+} ($r = 0.62$ Å) in the SMLW host which resulted in the expansion of the lattice on the basis of Bragg equation ($2d \sin\theta = \lambda$, where d, θ, and λ refer to crystal surface spacing, diffraction angle, and X-ray wavelength, respectively). The results further confirmed the above conclusion that Mn^{4+} ions can occupy the sites of W^{6+} ions.

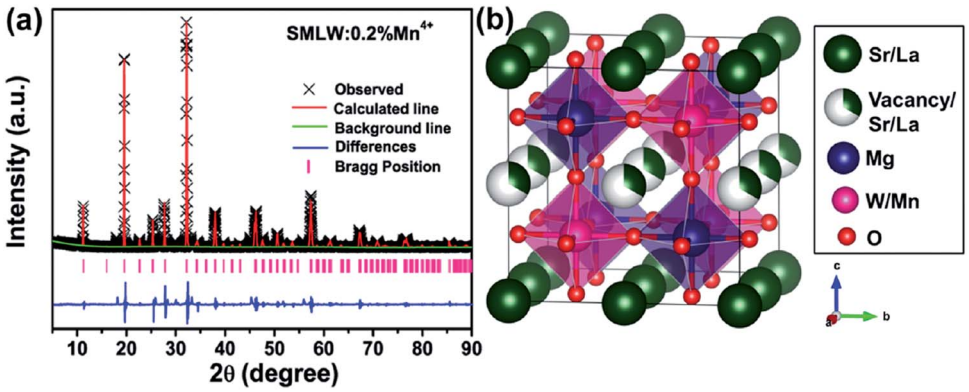

Fig. 1 (a) The Rietveld refinement for the XRD patterns of SMLW:0.2% Mn^{4+} phosphors. (b) The crystal structure of SMLW:0.2% Mn^{4+} phosphors.

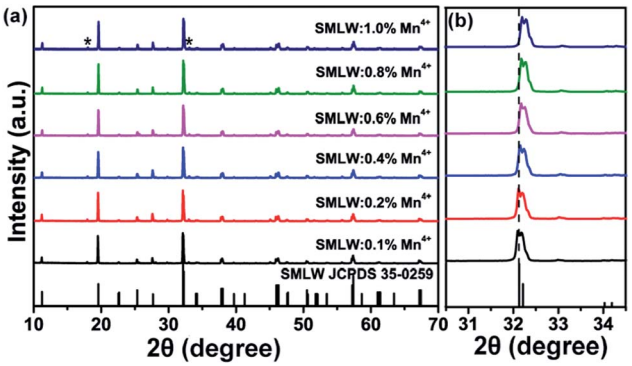

Fig. 2 (a) The XRD patterns of SMLW:xMn^{4+} (x = 0.1%, 0.2%, 0.4%, 0.6%, 0.8%, and 1.0%) phosphors and the standard PDF card SMLW (JCPDS # 35-0259). (b) The local XRD patterns in the 2θ range from 30.5 to 34.5 degree.

Fig. 3(a–c) shows the FE-SEM images of the SMLW:0.2% Mn^{4+} phosphors. The sample was made up of irregular micro-particles with the particle size ranging from 1 to 5 μm. The elemental mapping was shown in Fig. 3(d), according to which we can see that all the elements (O, Mg, La, W, Sr, and Mn) were uniformly distributed over the whole particles, which indicated that the SMLW:Mn^{4+} phosphors were successfully synthesized.

Fig. 4(a) exhibits the PLE and PL spectra of SMLW:0.2% Mn^{4+} phosphors. The PLE spectrum monitored at 708 nm showed a broad absorption band in the near-UV and blue regions ranging from 300–550 nm centered at 344 nm and 469 nm, respectively, which can be Gaussian fitted into four bands peaking at around 326 nm, 350 nm, 402 nm, and 479 nm, corresponding to the Mn–O charge transfer band (CTB), the $^4A_{2g} \rightarrow {}^4T_{1g}$, $^4A_{2g} \rightarrow {}^2T_{2g}$, and $^4A_{2g} \rightarrow {}^4T_{2g}$ transitions of Mn^{4+} ions, respectively.[44] The PL spectra excited at 344 nm and 469 nm with the similar profiles consisted of a narrow far-red emission band in the range of 650–780 nm peaking at around 708 nm,

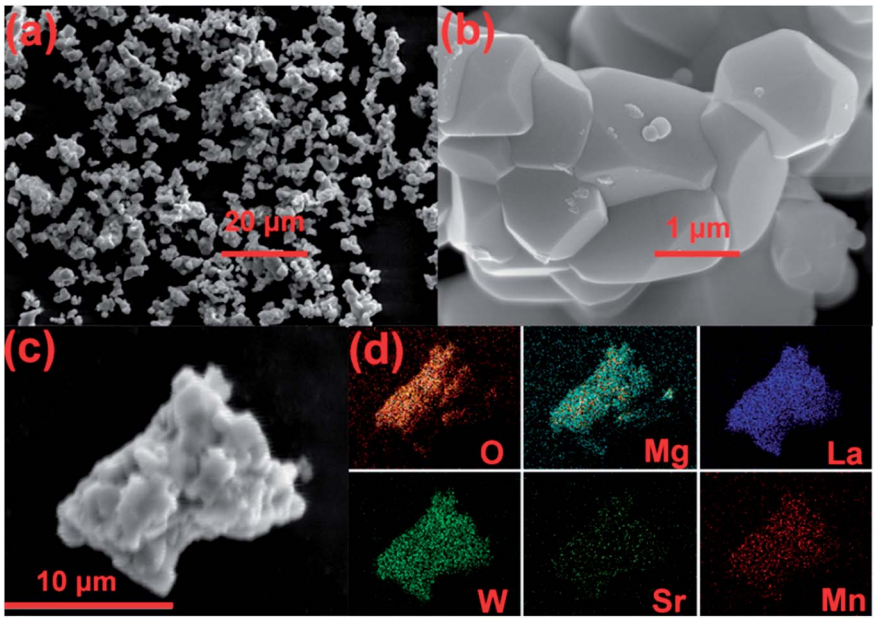

Fig. 3 (a–c) FE-SEM images and (d) elemental mapping of as-prepared SMLW:0.2% Mn^{4+} phosphors.

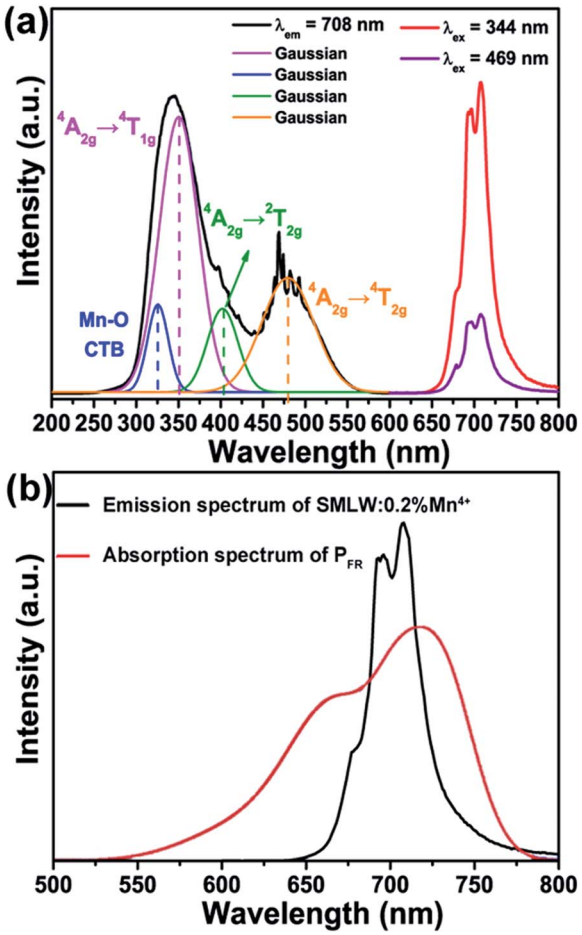

Fig. 4 (a) PLE (λ_{em} = 708 nm) and PL (λ_{ex} = 344 nm and 469 nm) spectra of SMLW:0.2% Mn^{4+} phosphors. (b) The emission spectrum of SMLW:0.2% Mn^{4+} and absorption spectrum of P_{FR}.

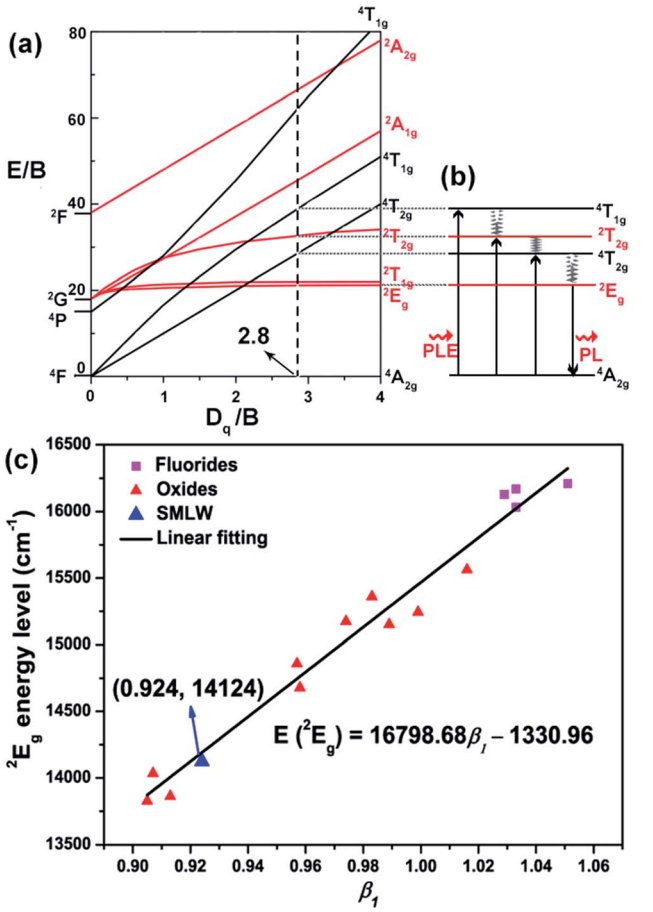

Fig. 5 (a) Tanabe–Sugano energy level diagram of Mn^{4+} ions in the SMLW host. (b) The simple energy level diagram of Mn^{4+} ions. (c) The relationship between the ^2E_g energy level of Mn^{4+} ions and the calculated nephelauxetic ratio β_1 in different hosts.

due to the $^2E_g \rightarrow {}^4A_{2g}$ transition of Mn^{4+} ions.[3] And the PL intensity of the SMLW:0.2% Mn^{4+} phosphors excited at 344 nm was much stronger than that excited at 469 nm. Furthermore, the emission spectrum of SMLW:0.2% Mn^{4+} and absorption spectrum of P_{FR} were shown in Fig. 4(b), and we can see that the far-red emission band of SMLW:0.2% Mn^{4+} matched well with the absorption band of phytochrome P_{FR}, indicating that the SMLW:Mn^{4+} phosphors were potential far-red emitting materials towards applications in LEDs for indoor plant cultivation. Besides, the full width at half maximum (FWHM) of the PL spectrum under the 344 nm excitation was about 37 nm.

Fig. 5(a) shows the Tanabe–Sugano energy level diagram, which can illustrate the electron transitions of Mn^{4+} ions corresponding to different energy levels in an octahedral crystal field. There are two important free ion states including ^2H excited level and ^4F ground level. The ^4F ground level can split into $^4A_{2g}$, $^4T_{2g}$, and $^4T_{1g}$ states, when excited at near-UV/blue light, the electrons at the ground state $^4A_{2g}$ transit to the excited states ($^4T_{1g}$, $^2T_{2g}(^2G)$, and $^4T_{2g}$) corresponding to the spin-allowed transitions $^4A_{2g} \rightarrow {}^4T_{1g}$, $^4A_{2g} \rightarrow {}^2T_{2g}$, and $^4A_{2g} \rightarrow {}^4T_{2g}$ respectively, then relax to the lowest excited state ^2E_g in a way of nonradiative transition, and finally come back to the ground state $^4A_{2g}$ through radiative transition ($^2E_g \rightarrow {}^4A_{2g}$), as can be described by a simple energy level diagram of Mn^{4+} ions in Fig. 5(b).

The crystal field strength (Dq) of Mn^{4+} can be calculated by the peak energy (20 876 cm^{-1}) of $^4A_{2g} \rightarrow {}^4T_{2g}$ transition according to the following equation:[45–47]

$$Dq = E(^4A_{2g}-{}^4T_{2g})/10 \quad (2)$$

The Racah parameter B can be roughly estimated on the basis of the energy difference (7695 cm^{-1}) between $^4A_{2g} \rightarrow {}^4T_{2g}$ and $^4A_{2g} \rightarrow {}^4T_{1g}$ transitions of Mn^{4+} ions using the formula as follows:

$$\frac{Dq}{B} = \frac{15(x-8)}{x^2-10x} \quad (3)$$

And the parameter x can be evaluated by the following formula:

$$x = \frac{E(^4A_{2g} - {}^4T_{1g}) - E(^4A_{2g} - {}^4T_{2g})}{Dq} \quad (4)$$

Besides, the Racah parameter C can be estimated according to the peak energy (14 124 cm^{-1}) of the $^2E_g \rightarrow {}^4A_{2g}$ transition of Mn^{4+} ions by the equation:

$$E(^2E_g–^4A_{2g})/B = 3.05C/B + 7.9 - 1.8B/Dq \quad (5)$$

On the basis of the above equations, the value of the parameter Dq, B, and C were calculated to be around 2088, 746, and 2856 cm^{-1}, respectively. Thus the value of Dq/B was determined to be about 2.8, which was higher than 2.2, indicating that Mn^{4+} ions occupied a strong crystal field in the SMLW host.[48]

According to the Tanabe–Sugano energy level diagram of Mn^{4+} ions, we can see that the energy of ^2E_g level has no relation with the crystal field strength.[49] Therefore, the emission wavelength of $^2E_g \rightarrow {}^4A_{2g}$ transition of Mn^{4+} ions does not vary with the crystal field strength, but depends on the nephelauxetic effect, which is attributed to the covalence between the Mn^{4+} ions and ligand.[27] In order to predict the emission wavelength of Mn^{4+} in different host, Brik *et al.* set up a dimensionless linear correlation by introducing a parameter of the nephelauxetic ratio (β_1):[15]

$$\beta_1 = \sqrt{\left(\frac{B}{B_0}\right)^2 + \left(\frac{C}{C_0}\right)^2} \quad (6)$$

where B, C, B_0, and C_0 represent the Racah parameter of Mn^{4+} ions, corresponding to 746, 2856, 1160, and 4303 cm^{-1}, respectively. Herein, β_1 can be calculated to be 0.924. Table 1 listed the value of β_1 and Mn^{4+}:^2E_g energy level in different hosts, and the well linear fitted plot of ^2E_g energy level *versus* β_1 was also shown in Fig. 5(c). Furthermore, the experimental value of the peak energy ($^2E_g \rightarrow {}^4A_{2g}$) of Mn^{4+} ions in SMLW host was 14 124 cm^{-1}, and when the coordinates (0.924, 14 124) of SMLW:Mn^{4+} were put into Fig. 5(c), they were well consistent with the fitted linear relation.

Fig. 6(a) presents the PL spectra of SMLW:$x$$Mn^{4+}$ (x = 0.1%, 0.2%, 0.4%, 0.6%, 0.8%, and 1.0%) phosphors under the 344 nm excitation. With the increasing concentration of Mn^{4+} ions, the PL intensity first increased to the maximum value and then gradually decreased because of the concentration quenching, which was attributed to the nonradiative energy transfer between Mn^{4+} ions.[50,51] Fig. 6(b) shows the emission intensity of SMLW:$x$$Mn^{4+}$ as a function of Mn^{4+} ions concentration at the wavelength 708 nm. It is intuitive to see that the optimal doping concentration of Mn^{4+} ions in the SMLW:$x$$Mn^{4+}$ was 0.2%. In addition, we can approximately calculate the critical distance R_c by using the following equation to estimate the nonradiative energy transfer mechanism between Mn^{4+} ions:

$$R_c = 2\left(\frac{3V}{4\pi x_c Z}\right)^{1/3} \quad (7)$$

where R_c is the critical distance, x_c represents the critical concentration, V refers to the volume of unit cell, and Z is the number of cation that can be occupied by activator ions per unit cell. For SMLW:0.2% Mn^{4+}, $x_c = 0.2\%$, $Z = 4$, and $V = 487.47$ Å^3, thus, the value of R_c was calculated to be around 48.83 Å. Moreover, the energy transfer between Mn^{4+} ions can occur by two interactions: exchange interaction and electric multipolar interaction.[52] The exchange interaction is dominant in the energy transfer only when the value of R_c is less than 5 Å. Since the R_c was 48.83 Å, which was much larger than 5 Å, so the nonradiative energy transfer between Mn^{4+} ions take place *via* electric multipolar interaction in SMLW:Mn^{4+} phosphors.

To further study the specific interaction in energy transfer mechanism, the relation between the $\log(I/x)$ and $\log(x)$ can be estimated by the formula as follows:[53]

$$\log(I/x) = A - (\theta/3)\log x \quad (8)$$

where I refers to the emission intensity, x is the doping concentration, A is a constant, θ = 3, 6, 8, and 10 corresponds to the nonradiative energy transfer among the nearest-neighbor ions,[54–57] electric dipole–dipole, dipole–quadrupole, and quadrupole–quadrupole interaction, respectively. The dependence of $\log(I/x)$ on $\log(x)$ was shown in Fig. 6(c). The data were linear fitted and the slope was determined to be around −1.274. Thus θ = 3.832, and it was close to 3, which suggested that the primary interaction responsible for energy transfer mechanism was the nonradiative energy transfer among the nearest-neighbor ions.

Table 1 The crystal field (Dq), Racah parameters (B, C), nephelauxetic ratio (β_1), and ^2E_g energy level ($E(^2E_g)$)of Mn^{4+} ions in different host

Host	Dq/cm^{-1}	B/cm^{-1}	C/cm^{-1}	β_1	$E(^2E_g)$/cm^{-1}	Ref.
Na_2SiF_6	2174	775	3475	1.051	16 210	63
Na_2SnF_6	2101	589	3873	1.033	16 171	64
K_2MnF_6	2183	604	3821	1.029	16 129	65
Cs_2GeF_6	2063	490	4056	1.033	16 032	66
$Y_2Sn_2O_7$	2100	700	3515	1.016	15 563	67
$CaAl_2O_{19}$	2132	807	3088	0.999	15 244	68
$SrMgAl_{10}O_{17}$	2237	791	3084	0.989	15 152	69
$Sr_4Al_{14}O_{25}$	2222	680	3397	0.983	15 361	70
Ba_2LaNbO_6	1780	670	3290	0.958	14 679	71
$Mg_{14}Ge_5O_{24}$	2375	709	3263	0.974	15 175	72
$LaAlO_3$	2123	695	2941	0.907	14 034	73
$BaTiO_3$	1780	738	2820	0.913	13 862	74
$SrTiO_3$	1818	719	2839	0.905	13 827	75
$SrMg_2La_2W_2O_{12}$	2088	746	2856	0.924	14 124	This work

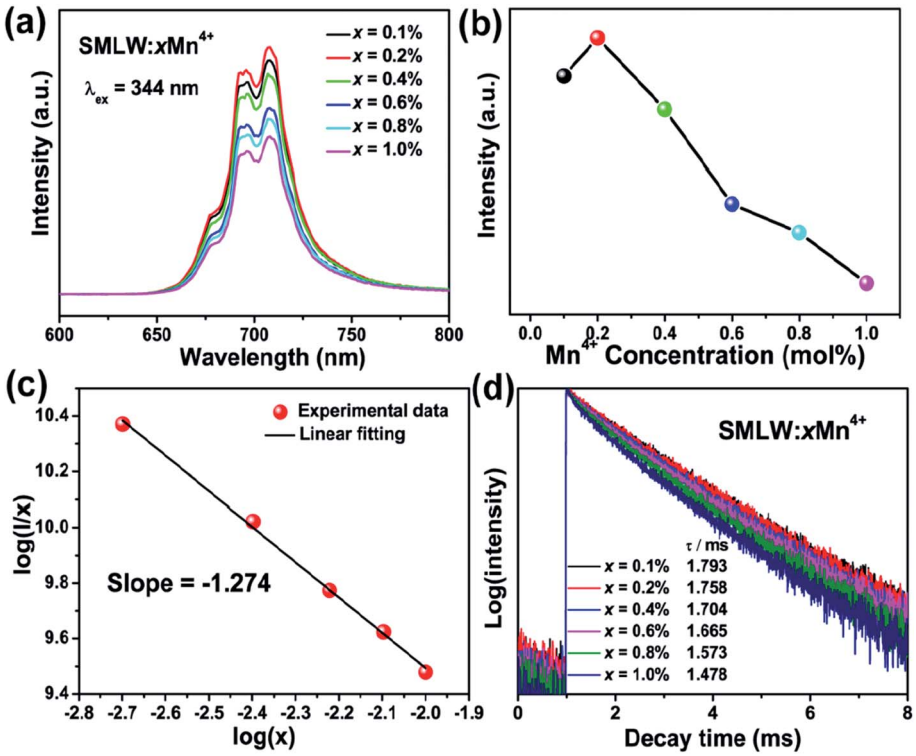

Fig. 6 (a) PL spectra of SMLW:xMn^{4+} (x = 0.1%, 0.2%, 0.4%, 0.6%, 0.8%, and 1.0%) phosphors excited at 344 nm. (b) The emission intensity of SMLW:xMn^{4+} as a function of Mn^{4+} doping concentration. (c) The dependence of log(I/x) on log(x). (d) The lifetime decay curves of SMLW:xMn^{4+} (x = 0.1%, 0.2%, 0.4%, 0.6%, 0.8%, 1.0%) phosphors under the 344 nm excitation while monitored at 708 nm.

Fig. 6(d) shows the lifetime decay curves of SMLW:xMn^{4+} (x = 0.1%, 0.2%, 0.4%, 0.6%, 0.8%, and 1.0%) phosphors excited at 344 nm and monitored at 708 nm. All the curves can be well fitted to second-exponential formula as follows:[28]

$$I = I_0 + A_1 \exp(-t/\tau_1) + A_2 \exp(-t/\tau_2) \quad (9)$$

where I refers to the emission intensity at time t, I_0 refers to the initial emission intensity, A_1 and A_2 are constants, and τ_1 and τ_2 represent the fast and slow lifetimes for the exponential segment. And the average decay times can be calculated by the following equation:

$$\tau = (A_1\tau_1^2 + A_2\tau_2^2)/(A_1\tau_1 + A_2\tau_2) \quad (10)$$

The average decay times of the SMLW:xMn^{4+} (x =0.1%, 0.2%, 0.4%, 0.6%, 0.8%, and 1.0%) phosphors were calculated to be 1.793, 1.758, 1.704, 1.665, 1.573, and 1.478 ms, respectively. It was clear to see that the decay times decreased gradually with the increasing concentration of Mn^{4+} ions for the reason that the energy transfer among Mn^{4+} ions became more frequent owing to the closer distance between Mn^{4+} ions with the increasing concentration.[58]

The CIE chromaticity coordinates diagram of SMLW:0.2% Mn^{4+} phosphors were shown in Fig. 7(a). The CIE chromaticity coordinates were calculated to be (0.7322, 0.2678) and it located in far-red region. Inset (i) and (ii) represent the photographs of the SMLW:0.2% Mn^{4+} sample under daylight and 365 nm near-UV light, respectively. It was clear to see that the as-prepared sample emitted bright red light excited at 365 nm. What's more, the excitation line of $BaSO_4$ reference and emission spectrum of SMLW:0.2% Mn^{4+} sample were shown in Fig. 7(b), and the IQE of this sample can be calculated according to the equation as follows:[59]

$$\eta = \frac{\int L_S}{\int E_R - \int E_S} \times 100\% \quad (11)$$

where η is the IQE, L_S refers to the emission spectrum of the sample, E_S and E_R are the excitation spectra with and without the sample, respectively. Thus, the value of IQE of SMLW:0.2% Mn^{4+} sample excited at 344 nm was found to be 88% which is much higher than that of some Mn^{4+} doped red phosphors reported previously such as $Ca_3La_2W_2O_{12}$:Mn^{4+} (IQE = 47.9%),[3] Gd_2ZnTiO_6:Mn^{4+} (IQE = 39.7%),[29] and Li_2MgZrO_4:Mn^{4+} (IQE = 32.3%),[60] indicating that the as-prepared SMLW:0.2% Mn^{4+} phosphors possessed a high luminescent efficiency which was beneficial to being applied in LEDs for indoor plant cultivation.

Fig. 8(a) shows the emission spectra of SMLW:0.2% Mn^{4+} phosphors under the 344 nm excitation at the temperature range from 303 to 503 K. There were no big changes in the profiles of the emission spectra at different temperature, but the PL intensity decreased gradually with the increasing of temperature owing to the thermal quenching effect for the

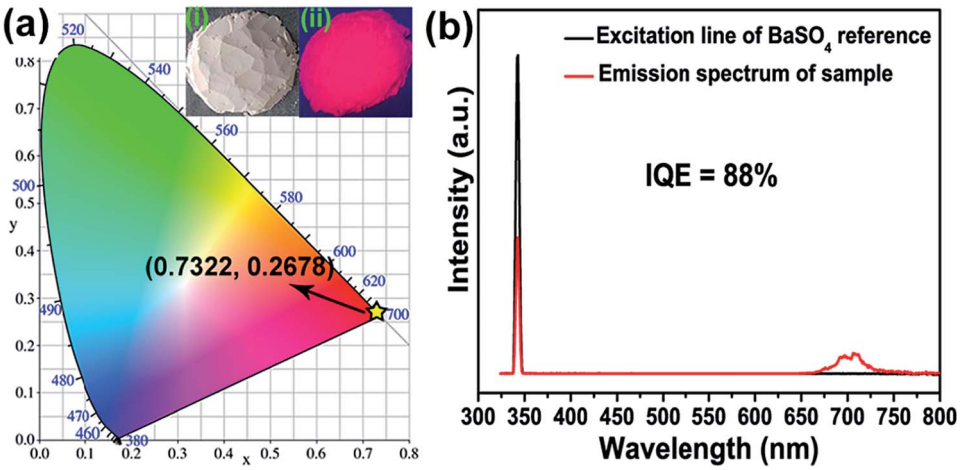

Fig. 7 (a) CIE chromaticity coordinates diagram of SMLW:0.2% Mn^{4+} phosphors (λ_{ex} = 344 nm). Inset (i) and (ii) represent the photographs of the SMLW:0.2% Mn^{4+} under daylight and 365 nm near-UV light, respectively. (b) The excitation line of $BaSO_4$ reference and the emission spectrum of SMLW:0.2% Mn^{4+} phosphors excited at 344 nm.

reason that the lattice relaxation of the luminescence center increased and the non-radiation transition became more possible with increasing the temperature.[39] Fig. 8(b) shows the normalized PL intensities of SMLW:0.2% Mn^{4+} phosphors at different temperature from 303 to 503 K. The emission intensity at 423 K still kept 57.5% of the initial value at 303 K, which was higher than that of some previously reported Mn^{4+}-activated phosphors, such as $CaYAlO_4$:Mn^{4+} (50%),[61] $La(MgTi)_{1/2}O_3$:Mn^{4+} (53%),[27] and Gd_2ZnTiO_6:Mn^{4+} (27.2%),[29] indicating that SMLW:0.2% Mn^{4+} phosphors possessed good thermal stability.

In addition, we can illustrate the mechanism of thermal quenching behavior by using a simple configuration diagram of Mn^{4+} ions shown in Fig. 8(c). Normally, when excited at near-UV/blue light, the electrons at the ground state $^4A_{2g}$ can transit to the excited states ($^4T_{1g}$, $^2T_{2g}$, and $^4T_{2g}$), then relax to the lowest excited state ^2E_g which is a process of nonradiative

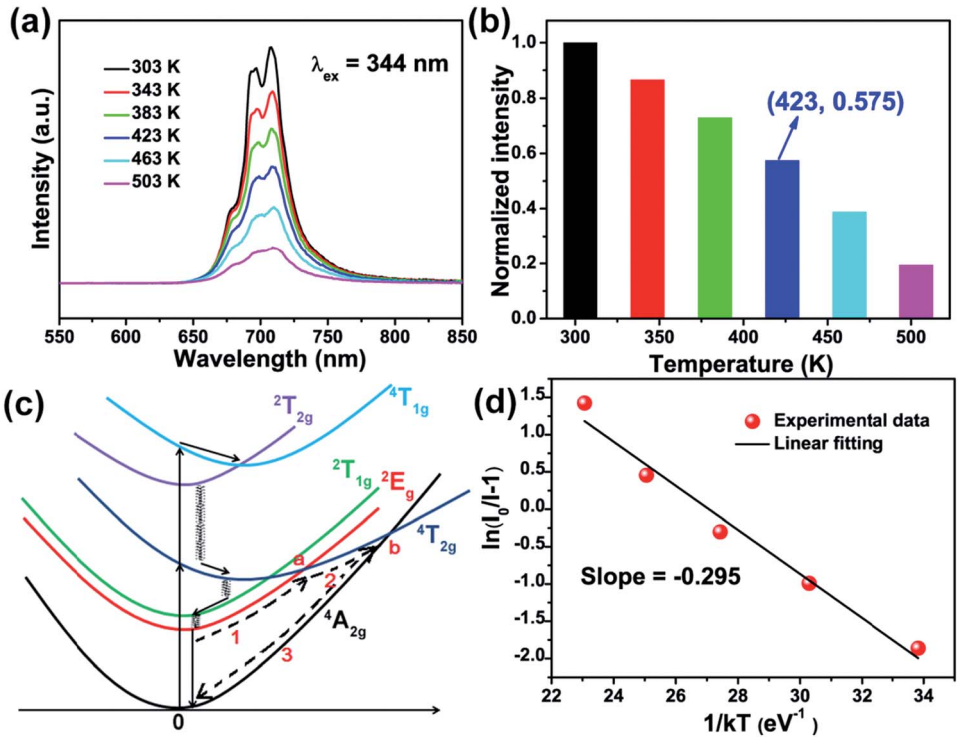

Fig. 8 (a) The temperature-dependent PL spectra of SMLW:0.2% Mn^{4+} phosphors. (b) The normalized PL intensities of SMLW:0.2% Mn^{4+} phosphors at different temperature from 303 to 503 K. (c) The configuration diagram of Mn^{4+} in the octahedron. (d) The plot of $\ln(I_0/I - 1)$ *versus* $1/kT$.

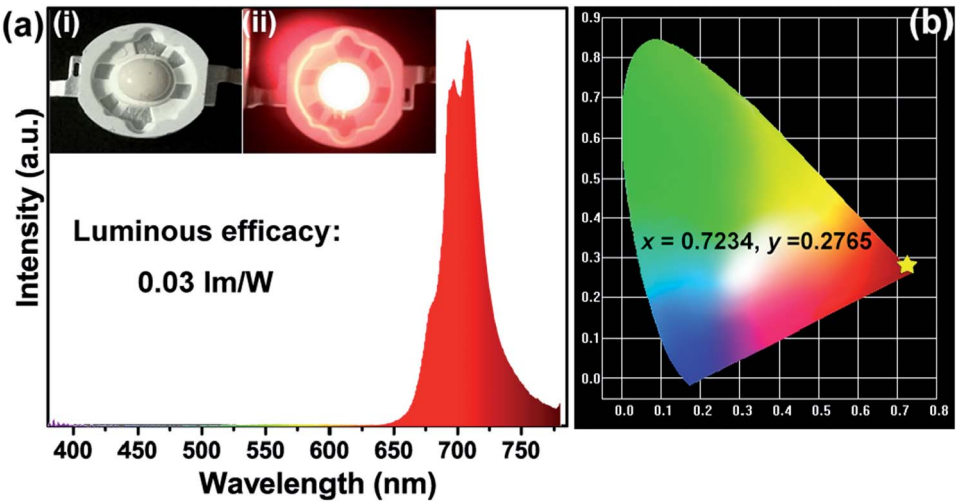

Fig. 9 (a) EL spectrum of fabricated far-red emitting LED lamp by using a 365 nm near-UV chip combined with SMLW:0.2% Mn^{4+} phosphors driven by 60 mA current. Inset (ii) and (i) were the photographs of the far-red LED lamp with and without current, respectively. (b) CIE chromaticity coordinates diagram based on the EL spectrum of fabricated far-red emitting LED lamp excited at 365 nm.

transition, and finally return to the ground state $^4A_{2g}$ through radiative transition accompanied with emitting far-red light. With increasing the temperature, part of electrons at excited state ^2E_g can be excited to the crossover point a and b, then return back to the ground state $^4A_{2g}$ which can be described through paths 1, 2, and 3, leading to lower probability of radiative transition $^2E_g \rightarrow {}^4A_{2g}$, and thus emission intensity of Mn^{4+} ions decreases with increasing the temperature.[23,27]

Furthermore, the value of activation energy (E_a) for thermal quenching can be calculated by using the following Arrhenius equation:[62]

$$I/I_0 = \left[1 + C\exp\left(\frac{-E_a}{kT}\right)\right]^{-1} \quad (12)$$

where I_0 is the initial emission intensity at 303 K; I is the emission intensity at different temperature ranging from 303 to 503 K; C is a constant; k is the Boltzmann constant (8.62×10^{-5} eV); and E_a is the activation energy for thermal quenching. The plot of the $\ln(I_0/I - 1)$ *versus* $1/kT$ was exhibited in Fig. 8(d). The experimental data can be well linear fitted and the slope was −0.295, indicating that the value of activation energy was 0.295 eV.

Moreover, a far-red emitting LED lamp was fabricated by using a 365 nm near-UV LED chip combined with the as-synthesized SMLW:0.2% Mn^{4+} far-red phosphors. Fig. 9(a) shows the electroluminescence (EL) spectrum of the fabricated red-emitting LED driven by 60 mA current. Inset (ii) and inset (i) were the photographs of the far-red LED lamp with and without current, respectively, and it exhibited bright far-red light under the 60 mA current. In addition, we can see that the spectrum excited at 365 nm consisted of a narrow far-red emission band peaking at around 708 nm ranging from 650–780 nm due to the $^2E_g \rightarrow {}^4A_{2g}$ transition of Mn^{4+} ions, which matched well with the PL spectrum of SMLW:0.2Mn^{4+} phosphors under the 344 nm excitation mentioned above. The CIE chromaticity coordinates based on the EL spectrum of the fabricated far-red emitting LED were calculated to be (0.7234, 0.2765), which located in far-red region as shown in Fig. 9(b). The luminous efficacy of this lamp, which can represent the sensitivity of human eyes to light, was determined to be 0.03 lm W^{-1}. In this work, the fabricated far-red emitting LED used for indoor plant cultivation emitted far-red light (~708 nm) and the perception ability of human eyes to far-red light is relatively weak, indicating that the low luminous efficacy of this lamp is reasonable. These results suggested that the SMLW:Mn^{4+} phosphors were promising far-red emitting luminescent materials applied in LEDs for indoor plant growth.

4. Conclusions

Overall, novel Mn^{4+}-activated SMLW phosphors were prepared by a traditional high-temperature solid-state reaction method. The as-synthesized SMLW:Mn^{4+} phosphors can be excited at 344 nm or 469 nm and exhibited a far-red emission band in the 650–780 nm range centered at about 708 nm, which matched well with the absorption band of phytochrome P_{FR}. And the FWHM of the far-red emission band was about 37 nm. The optimal Mn^{4+} concentration in SMLW:$x$$Mn^{4+}$ was x = 0.2%, and the CIE chromaticity coordinates of SMLW:0.2% Mn^{4+} phosphors were calculated to be (0.7322, 0.2678). Besides, the crystal field strength Dq, Racah parameters B and C, as well as the nephelauxetic ratio β_1 of SMLW:Mn^{4+} phosphors were estimated to analyze the influences of crystal field strength and nephelauxetic effect on the emission energy of Mn^{4+} ions. Moreover, the IQE of SMLW:0.2% Mn^{4+} phosphors reached as high as 88%. Importantly, the emission intensity at 423 K was still 57.5% of the initial value at 303 K, indicating that the SMLW:0.2% Mn^{4+} phosphors possessed good thermal stability. Finally, a far-red LED lamp was fabricated by using a 365 nm near-UV emitting LED chip combined with the SMLW:0.2% Mn^{4+} far-red phosphors. Consequently, the as-synthesized SMLW:0.2% Mn^{4+} sample was promising far-red phosphors applied in LEDs as artificial light source for indoor plant growth.

Conflicts of interest

There are no conflicts to declare.

Acknowledgements

This work was supported by the National Natural Science Foundation of China (No. 51502190), the Program for the Outstanding Innovative Teams of Higher Learning Institutions of Shanxi, and the Open Fund of the State Key Laboratory of Luminescent Materials and Devices (South China University of Technology, No. 2017-skllmd-01).

References

1 R. Cao, Y. Ye, Q. Peng, G. Zheng, H. Ao, J. Fu, Y. Guo and B. Guo, *Dyes Pigm.*, 2017, **146**, 14–19.
2 R. Cao, Z. Shi, G. Quan, T. Chen, S. Guo, Z. Hu and P. Liu, *J. Lumin.*, 2017, **188**, 577–581.
3 X. Huang and H. Guo, *Dyes Pigm.*, 2018, **152**, 36–42.
4 C. Yang, Z. Zhang, G. Hu, R. Cao, X. Liang and W. Xiang, *J. Alloys Compd.*, 2017, **694**, 1201–1208.
5 R. Cao, J. Zhang, W. Wang, Z. Hu, T. Chen, Y. Ye and X. Yu, *Mater. Res. Bull.*, 2017, **87**, 109–113.
6 J. Chen, N. Zhang, C. Guo, F. Pan, X. Zhou, H. Suo, X. Zhao and E. M. Goldys, *ACS Appl. Mater. Interfaces*, 2016, **8**, 20856–20864.
7 L. Li, Y. Pan, Z. Chen, S. Huang and M. Wu, *RSC Adv.*, 2017, **7**, 14868–14875.
8 X. Huang, S. Wang, B. Li, Q. Sun and H. Guo, *Opt. Lett.*, 2018, **43**, 1307–1310.
9 X. Huang, H. Guo and B. Li, *J. Alloys Compd.*, 2017, **720**, 29–38.
10 X. Huang, B. Li, H. Guo and D. Chen, *Dyes Pigm.*, 2017, **143**, 86–94.
11 X. Huang, B. Li and H. Guo, *J. Alloys Compd.*, 2017, **695**, 2773–2780.
12 R. Cao, Z. Shi, G. Quan, Z. Luo, P. Tang, H. Ao and X. Yu, *Opt. Mater.*, 2016, **57**, 212–216.
13 H. Guo, X. Huang and Y. Zeng, *J. Alloys Compd.*, 2018, **741**, 300–306.
14 H. Guo, B. Devakumar, B. Li and X. Huang, *Dyes Pigm.*, 2018, **151**, 81–88.
15 B. Li and X. Huang, *Ceram. Int.*, 2018, **44**, 4915–4923.
16 B. Li, X. Huang, H. Guo and Y. Zeng, *Dyes Pigm.*, 2018, **150**, 67–72.
17 M. Zhao, Z. Xia, M. S. Molokeev, L. Ning and Q. Liu, *Chem. Mater.*, 2017, **29**, 6552–6559.
18 J. Qiao, Z. Xia, Z. Zhang, B. Hu and Q. Liu, *Sci. China Mater.*, 2018, **61**, 985–992.
19 J. Qiao, L. Ning, M. S. Molokeev, Y. C. Chuang, Q. Liu and Z. Xia, *J. Am. Chem. Soc.*, 2018, **140**, 9730–9736.
20 P. Du, L. Luo, X. Huang and J. S. Yu, *J. Colloid Interface Sci.*, 2018, **514**, 172–181.
21 X. Huang, *J. Alloys Compd.*, 2017, **690**, 356–359.
22 P. Du, X. Huang and J. S. Yu, *Inorg. Chem. Front.*, 2017, **4**, 1987–1995.
23 A. Fu, L. Zhou, S. Wang and Y. Li, *Dyes Pigm.*, 2018, **148**, 9–15.
24 L. Qin, S. Bi, P. Cai, C. Chen, J. Wang, S. I. Kim, Y. Huang and H. J. Seo, *J. Alloys Compd.*, 2018, **755**, 61–66.
25 J. Xiang, J. Chen, N. Zhang, H. Yao and C. Guo, *Dyes Pigm.*, 2018, **154**, 257–262.
26 Y. Zheng, H. Zhang, H. Zhang, Z. Xia, Y. Liu, M. S. Molokeev and B. Lei, *J. Mater. Chem. C*, 2018, **6**, 4217–4224.
27 Z. Zhou, J. Zheng, R. Shi, N. Zhang, J. Chen, R. Zhang, H. Suo, E. M. Goldys and C. Guo, *ACS Appl. Mater. Interfaces*, 2017, **9**, 6177–6185.
28 S. S. Liang, M. M. Shang, H. Z. Lian, K. Li, Y. Zhang and J. Lin, *J. Mater. Chem. C*, 2016, **4**, 6409–6416.
29 H. Chen, H. Lin, Q. Huang, F. Huang, J. Xu, B. Wang, Z. Lin, J. Zhou and Y. Wang, *J. Mater. Chem. C*, 2016, **4**, 2374–2381.
30 Q. Sun, B. Li, S. Wang, H. Guo and X. Huang, *J. Mater. Sci.: Mater. Electron.*, 2018, **29**, 12972–12977.
31 J. Liang, L. Sun, B. Devakumar, S. Wang, Q. Sun, H. Guo, B. Li and X. Huang, *RSC Adv.*, 2018, **8**, 27144–27151.
32 Q. Sun, S. Wang, B. Li, H. Guo and X. Huang, *J. Lumin.*, 2018, **203**, 371–375.
33 Q. Sun, S. Wang, B. Devakumar, B. Li, L. Sun, J. Liang and X. Huang, *RSC Adv.*, 2018, **8**, 28538–28545.
34 G. Blasse, *J. Solid State Chem.*, 1975, **14**, 181–184.
35 X. Huang, B. Li, P. Du, H. Guo, R. Cao, J. S. Yu, K. Wang and X. W. Sun, *Dyes Pigm.*, 2018, **151**, 202–210.
36 P. Du, L. Krishna Bharat and J. S. Yu, *J. Alloys Compd.*, 2015, **633**, 37–41.
37 R. Cao, X. Ceng, J. Huang, X. Xia, S. Guo and J. Fu, *Ceram. Int.*, 2016, **42**, 16817–16821.
38 X. Huang, J. Liang, B. Li, L. Sun and J. Lin, *Opt. Lett.*, 2018, **43**, 3305–3308.
39 K. Pavani, J. Suresh Kumar and L. Rama Moorthy, *J. Alloys Compd.*, 2014, **586**, 722–729.
40 K. Pavani, J. Suresh Kumar, L. Rama Moorthy and A. Srivastava, *J. Am. Ceram. Soc.*, 2014, **97**, 1481–1488.
41 K. Pavani, J. Suresh Kumar and L. Rama Moorthy, *Mater. Res. Express*, 2014, **1**, 016201.
42 R. Cao, X. Ceng, J. Huang, H. Ao, G. Zheng, X. Yu and X. Zhang, *Opt. Mater.*, 2016, **62**, 706–710.
43 K. Li, H. Lian and R. V. Deun, *J. Lumin.*, 2018, **198**, 155–162.
44 A. Fu, C. Zhou, Q. Chen, Z. Lu, T. Huang, H. Wang and L. Zhou, *Ceram. Int.*, 2017, **43**, 6353–6362.
45 S. Zhang, Y. Hu, H. Duan, Y. Fu and M. He, *J. Alloys Compd.*, 2017, **693**, 315–325.
46 S. J. Kim, H. S. Jang, S. Unithrattil, Y. H. Kim and W. B. Im, *J. Lumin.*, 2016, **172**, 99–104.
47 F. Baur and T. Jüstel, *J. Lumin.*, 2016, **177**, 354–360.
48 M. G. Brik, S. J. Camardello and A. M. Srivastava, *ECS J. Solid State Sci. Technol.*, 2014, **4**, R39–R43.
49 Y. Jin, Y. Hu, H. Wu, H. Duan, L. Chen, Y. Fu, G. Ju, Z. Mu and M. He, *Chem. Eng. J.*, 2016, **288**, 596–607.
50 S. Wang, Q. Sun, B. Li, H. Guo and X. Huang, *Dyes Pigm.*, 2018, **157**, 314–320.
51 J. Liang, P. Du, H. Guo, L. Sun, B. Li and X. Huang, *Dyes Pigm.*, 2018, **157**, 40–46.
52 H. Guo and X. Huang, *J. Alloys Compd.*, 2018, **764**, 809–814.
53 P. Du and J. S. Yu, *Dyes Pigm.*, 2017, **147**, 16–23.

54 Q. Shao, H. Ding, L. Yao, J. Xu, C. Liang and J. Jiang, *RSC Adv.*, 2018, **8**, 12035–12042.
55 H. Deng, Z. Gao, N. Xue, J. H. Jeong and R. Yu, *J. Lumin.*, 2017, **192**, 684–689.
56 R. Yu, H. M. Noh, B. K. Moon, B. C. Choi, J. H. Jeong, K. Jang, S. S. Yi and J. K. Jang, *J. Alloys Compd.*, 2013, **576**, 236–241.
57 H. Li, R. Zhao, Y. Jia, W. Sun, J. Fu, L. Jiang, S. Zhang, R. Pang and C. Li, *ACS Appl. Mater. Interfaces*, 2014, **6**, 3163–3169.
58 K. Li, H. Lian and R. V. Deun, *Dalton Trans.*, 2017, **47**, 2501–2505.
59 P. Du, X. Huang and J. S. Yu, *Chem. Eng. J.*, 2018, **337**, 91–100.
60 R. Cao, Z. Shi, G. Quan, T. Chen, S. Guo, Z. Hu and P. Liu, *J. Lumin.*, 2017, **188**, 577–581.
61 Y. Chen, M. Wang, J. Wang, M. Wu and C. Wang, *J. Solid State Light.*, 2014, **1**, 15.
62 B. Li, S. Wang, Q. Sun, C. Lu, H. Guo and X. Huang, *Dyes Pigm.*, 2018, **154**, 252–256.
63 Y. Xu and S. Adachi, *J. Appl. Phys.*, 2009, **105**, 013525.
64 Y. Arai and S. Adachi, *J. Lumin.*, 2011, **131**, 2652–2660.
65 R. Kasa, Y. Arai, T. Takahashi and S. Adachi, *J. Appl. Phys.*, 2010, **108**, 113503.
66 E. Lifshitz and A. H. Francis, *Chem. Phys.*, 1988, **127**, 297–304.
67 M. G. Brik, A. M. Srivastava and N. M. Avram, *Opt. Mater.*, 2011, **33**, 1671–1676.
68 T. Murata, T. Tanoue, M. Iwasaki, K. Morinaga and T. Hase, *J. Lumin.*, 2005, **114**, 207–212.
69 L. Meng, L. Liang and Y. Wen, *J. Mater. Sci.: Mater. Electron.*, 2014, **25**, 2676–2681.
70 Y. D. Xu, D. Wang, L. Wang, N. Ding, M. Shi, J. G. Zhong and S. Qi, *J. Alloys Compd.*, 2013, **550**, 226–230.
71 A. M. Srivastava and M. G. Brik, *J. Lumin.*, 2012, **132**, 579–584.
72 T. M. Chen and J. T. Luo, *US Pat.* no. 7, 2010, vol. 846, p. 350.
73 A. M. Srivastava and M. G. Brik, *Opt. Mater.*, 2013, **35**, 1544–1548.
74 X. Wu, W. Fang, W. Feng and W. Zheng, *Pramana*, 2009, **72**, 569–575.
75 Z. Bryknar, V. Trepakov, Z. Potucek and L. Jastrabík, *J. Lumin.*, 2000, **87–89**, 605–607.